ISSN 0021-3640, JETP Letters, 2016, Vol. 103, No. 4, pp. 248–253. © Pleiades Publishing, Inc., 2016.

CONDENSED MATTER

Room-Temperature Electric Polarization Induced by Phase Separation in Multiferroic $GdMn_2O_5$[1]

B. Kh. Khannanov, V. A. Sanina, E. I. Golovenchits, and M. P. Scheglov

Ioffe Institute, Russian Academy of Sciences, St. Petersburg, 194021 Russia

e-mail: sanina@mail.ioffe.ru

Received December 10, 2015; in final form, December 27, 2015

It was generally accepted until recently that multiferroics RMn_2O_5 crystallized in the centrosymmetric space group *Pbam* and ferroelectricity in them could exist only at low temperatures due to the magnetic exchange striction. Recent comprehensive structural studies [V. Baledent et al., Phys. Rev. Lett. **114**, 117601 (2015)] have shown that the actual symmetry of RMn_2O_5 at room temperature is a noncentrosymmetric monoclinic space group *Pm*, which allows room temperature ferroelectricity to exist. However, such a polarization has not yet been found. Our electric polarization loop studies of $GdMn_2O_5$ have revealed that a polarization does exist up to room temperature. This polarization occurs mainly in restricted polar domains that arise in the initial $GdMn_2O_5$ matrix due to phase separation and charge carrier self-organization. These domains are self-consistent with the matrix, which leads to the noncentrosymmetricity of the entire crystal. The polarization is controlled by a magnetic field, thereby demonstrating the presence of magnetoelectric coupling. The low-temperature ferroelectricity enhances the restricted polar domain polarization along the *b* axis.

DOI: 10.1134/S002136401604007X

1. INTRODUCTION

Manganites RMn_2O_5 (R is the rare earth ion) are typical multiferroics in which ferroelectricity is induced by a magnetic order. Characteristic Curie (T_C) and Neel (T_N) temperatures are 30–35 and 40–45 K, respectively [1–5]. It was believed until recently that RMn_2O_5 crystallized in the space group *Pbam* at room temperature and had a series of magnetic transitions at low temperatures [6]. The space group *Pbam* is centrosymmetric, and electric polarization is impossible. The polarization along the *b* axis is observed at low temperatures below the magnetic transition. To describe this ferroelectric order, the exchange striction mechanism caused by charge ordering of Mn^{3+} and Mn^{4+} ion pairs along the *b* axis [7] is typically used.

The study of structural properties of the room-temperature paramagnetic phase of RMn_2O_5 has recently shown that the actual space group is not centrosymmetric *Pbam* [8]. The authors could not give preference to any of two possible monoclinic space groups: *Pm* (with the polarization in the (*ab*) plane) and *P*2 (with the polarization along the *c* axis) on the basis of structural data. So they relied on the assumption that the polarization in RMn_2O_5 was bound to be oriented along the *b* axis at all temperatures and supposed that the symmetry was of the *Pm* type. Since the inversion symmetry of RMn_2O_5 is already broken at room temperature, the electrical polarization is bound to exist at this temperature. However, such polarization has not yet been detected.

We show in this Letter that the electric polarization does exist up to room temperature in $GdMn_2O_5$ (GMO) and discuss the origin of such a polarization. We present the polarization hysteresis loops for GMO which demonstrate the existence of electric polarization (P) along the *a*, *b*, and *c* axes in the paramagnetic phase. P_c is observed above room temperature. In addition, the study of the intensity distribution of Bragg reflections by a high-sensitivity three-crystal X-ray diffraction technique demonstrates a series of equivalent (004) Bragg reflections at room temperature. We believe that both the polarization and splitting of Bragg reflections are induced by phase separation and charge carrier self-organization, which give rise to restricted polar domains (RPD) in the initial crystal matrix. These domains are self-consistent with the matrix, which leads to the noncentrosymmetricity of the entire crystal.

Phase separation and charge carrier self-organization are typical of manganites containing Mn^{3+} and Mn^{4+} ions [9, 10]. Indeed, the unit cell of RMn_2O_5 contains a Mn^{3+} and a Mn^{4+} ion. Mn^{4+} ions ($t_{2g}^3 e_g^0$) occupy positions $z = 0.25c$ and $1 - z = 0.75c$ in the octahedral oxygen surrounding. Mn^{3+} ions ($t_{2g}^3 e_g^1$) are in positions $z = 0.5c$ in the pyramids formed by five

[1] The article is published in the original.

oxygen ions. Ions in RMn_2O_5 lie in the layers normal to the c axis [6]. Thus, RMn_2O_5 contain equal quantities of Mn^{3+} and Mn^{4+} ions. The distribution of these ions in the crystal and their recharging by e_g valence electrons (magnetic double exchange [9, 11]) play a key role in the RMn_2O_5 properties. Dielectric and magnetic properties of $EuMn_2O_5$ and $EuCeMn_2O_5$ [12–15] and $GdMn_2O_5$ and $GdCeMn_2O_5$ [16, 17] were earlier studied in a temperature range of 5–330 K. It was found that these properties were determined by the RPD originating from phase separation and charge carrier self-organization. The self-consistency of RPD and RMn_2O_5 initial matrix in the form of 2D superstructures normal to the c axis manifests itself in the most pronounced manner in $EuMn_2O_5$. The superstructure period at room temperature was found to be ≈900 Å [12, 13].

Among the RMn_2O_5 compounds, $GdMn_2O_5$ is of special interest due to properties of the ground state ${}^8S_{7/2}$ of Gd^{3+} ions, which weakly interact with the lattice but cause a strong uniform Gd–Mn exchange. This exchange enhances the polar order along the b axis at $T < 30$ K [18]. The weak interaction of Gd^{3+} ions with the lattice, in contrast to other R ions in RMn_2O_5, allows the Mn-subsystem contribution to electric polarization to be separated out.

2. EXPERIMENTAL DATA AND ANALYSIS

Single crystals of GMO were grown by the spontaneous crystallization technique described in [19, 20]. The as-grown single crystals were in the form of 2–3 mm thick plates with areas of 3–5 mm^2. To measure the polarization, capacitors with a thickness of 0.3–0.6 mm and area of 3–4 mm^2 were used. The polarization hysteresis loops were obtained by using the so-called positive-up negative-down (PUND) method [21–23]. We used the variant of the PUND method presented in [23], which was adapted to our measurements (see Fig. 1). If the sample has a relatively high conductivity (which is important for GMO containing RPD with local conductivities), the shape of the polarization-electric field (P–E) hysteresis loop is distorted and does not give information on the intrinsic P (panel (a) in Fig. 1). In the PUND method, only the hysteresis of P can be extracted by applying a series of voltage pulses to the sample. During successive $P1$–$P2$ and $N1$–$N2$ pulses, independent curves ($P1$–$P2$ and $N1$–$N2$) of effective P changes are registered (panel b in Fig. 1). The PUND method is based on the difference between polarization and conductivity responses to variations in the field E. The time intervals between $P1$–$P2$ and $N1$–$N2$ pulses should be chosen such that the intrinsic P is still unrelaxed while the conductivity relaxation is complete. In the conventional volume ferroelectrics with the domain structure, such time intervals may be up to two seconds. In our case, the

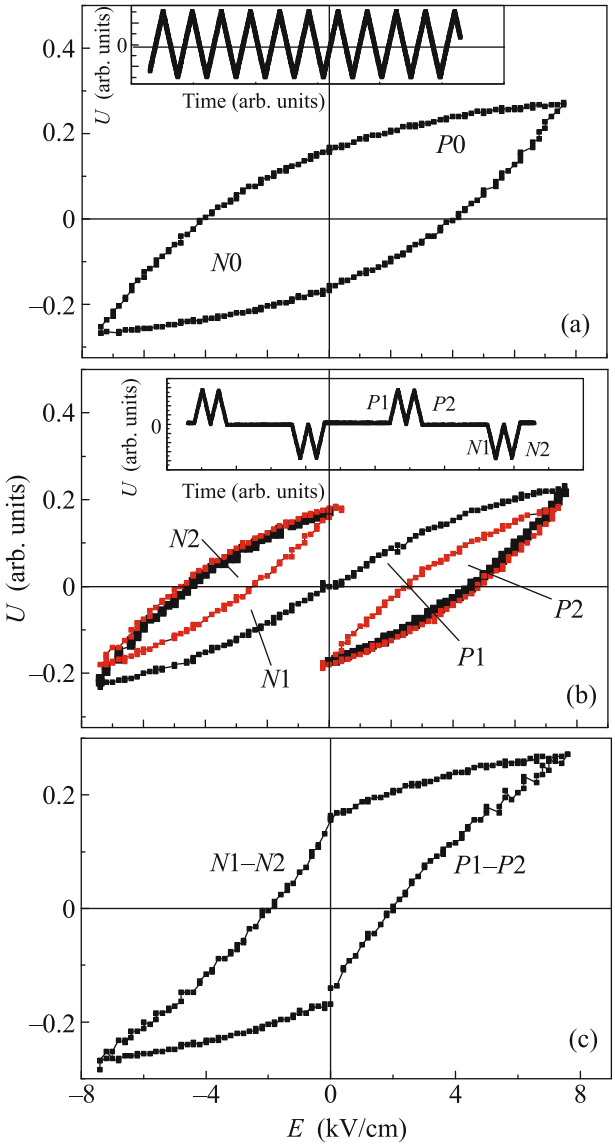

Fig. 1. (Color online) The PUND method for measurements of polarization hysteresis loops used in our experiments.

intrinsic P response was determined by the RPD, which rather rapidly restored after the field E was switched off. The reason for this will be discussed below. As a result, the time intervals between the $P1$–$P2$ and $N1$–$N2$ pulses were chosen so that the responses to the $P1$ and $N1$ pulses were irreversible (due to the intrinsic P contribution) and the conductivity responses to the $P2$ and $N2$ pulses were closed and reversible (see panel b in Fig. 1). This could be achieved if the time intervals between the $P1$–$P2$ and $N1$–$N2$ pulses did not exceed 0.8 ms. In our case the $P1$ and $N1$ curves reproduced the $P0$ and $N0$ ones and characterized the total P and conductivity contributions. To obtain the actual P–E loop, we subtracted the $P2$ and $N2$ curves from the $P0$–$N0$ curves (panel c

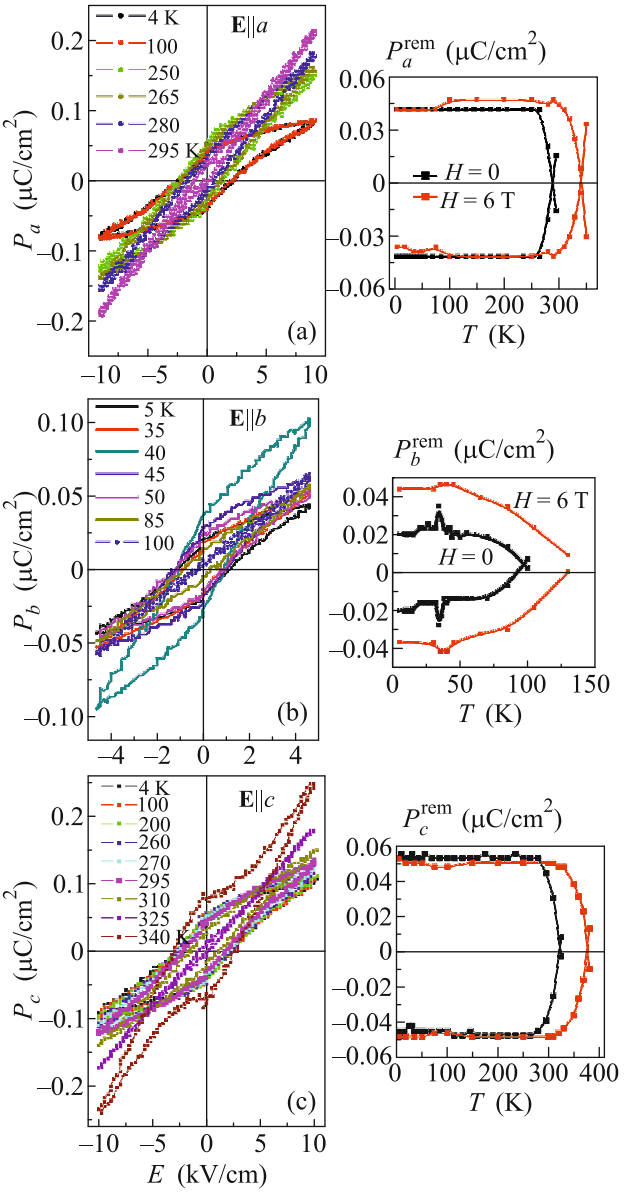

Fig. 2. (Color online) Polarization hysteresis loops (left panels) at different temperatures for $\mathbf{E} \parallel a$ (a), $\mathbf{E} \parallel b$ (b), and $\mathbf{E} \parallel c$ (c). Temperature dependences of remanent polarization in magnetic fields $H = 0$ and 6 T are shown in right panels.

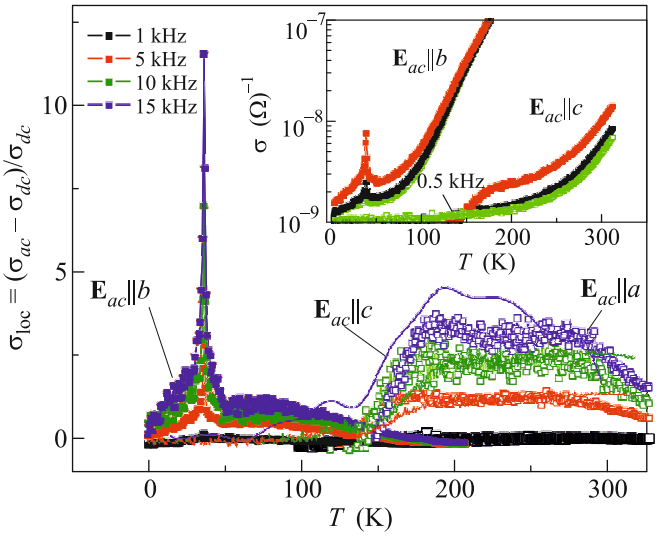

Fig. 3. (Color online) Temperature dependences of σ_{loc} along the (open symbols) *a*, (closed symbols) *b*, and (lines) *c* axes for different frequencies. The inset shows temperature dependences of conductivity along the *b* and *c* axes for different frequencies.

in Fig. 1). The duration of each pulse in the *P*1–*P*2 and *N*1–*N*2 series was 2 ms, the interval between the pulse series was 4 ms (see Fig. 1). Conductivity was measured by a Good Will LCR-819 impedance meter in the frequency range 0.5–50 kHz at 5–350 K. The intensity distributions of Bragg reflections for GMO were studied with a high-sensitivity three-crystal X-ray diffractometer. Figure 2 shows the *P*–*E* hysteresis loops of GMO in *E* oriented along the *a*, *b*, and *c* axes (left panels in Figs. 2a–2c, respectively). The right panels in these figures demonstrate temperature dependences of remanent polarization (P^{rem}). Hysteresis loops are observed for all three axes in a wide temperature interval from 5 K up to certain temperatures depending on the axis direction. The maximum P^{rem} that exists up to ~ 325 K is observed along the *c* axis. Similar but somewhat lower values are observed along the *a* axis. The minimum P^{rem} that exists up to ~100 K is along the *b* axis. Thus, P^{rem} and hysteresis loops of GMO, which demonstrate a strong anisotropy, are revealed in the paramagnetic phase along all crystal axes. We attribute P^{rem} and hysteresis loops mainly to the RPD, which emerge inside the initial matrix.

The inset in Fig. 3 shows temperature dependences of conductivities along the *b* and *c* axes at different frequencies. The conductivity along the *a* axis is close to the conductivity along the *c* axis. It is evident that these conductivities exhibit a strong anisotropy. We deal with the real conductivity $\sigma_1 = \omega\varepsilon''\varepsilon_0$ [24], which is calculated from dielectric losses ε'' (ω is an angular frequency, ε_0 is the dielectric permittivity ε' at ω = 0). This conductivity depends on both the frequency and temperature. The low-frequency conductivities are dispersion-free (percolation conductivity σ_{dc}). The conductivity σ_{ac} has a frequency dispersion: the higher the frequency, the higher the conductivity. The frequency dispersion of this type is typical of local conductivity (i.e., dielectric losses) in the restricted domains [24]. In our case, we attributed this local conductivity to RPD. The percolation conductivity (leakage) is attributed to the initial crystal matrix. The relative local conductivity $\sigma_{loc} = (\sigma_{ac} - \sigma_{dc})/\sigma_{dc}$ characterizes the ratio between the RPD local conductivity and the matrix percolation conductivity. Figure 3 demonstrates the temperature intervals in which σ_{loc} of the

RPD exceeds considerably the leakage and contributes significantly to the $P2$ and $N2$ curves. In the same temperature intervals both the intrinsic polarization and σ_{loc} contribute to the $P1$ and $N1$ curves. At these temperatures P^{rem} are nearly temperature-independent (see right panels in Fig. 2). At the temperatures at which P^{rem} tends to zero (the P^{rem} screening temperatures T_{scr}), the polarization and local conductivity contributions to the $P1-P2$ and $N1-N2$ curves start to decrease. At the temperatures at which $P^{rem} = 0$, these contributions are transformed into linear dependences on E. We believe that the thermal activation kinetic energy of the itinerant electrons at $T = T_{scr}$ becomes comparable to the RPD barrier height. At $T > T_{scr}$ the loop restores as an inverted loop, and the leakage contribution begins to dominate in it (see Fig. 2c for $T =$ 325 and 340 K). Figure 3 shows a strong anisotropy of σ_{loc} and leakage. The relative σ_{loc} along the b axis for $\sigma_{ac} \approx 10^{-9}-10^{-7}$ $(\Omega\ \text{cm})^{-1}$ manifests itself up to $T \approx$ 150 K. At $T >$ 150 K, there is only leakage, which grows with the temperature. Along the a and c axes, σ_{ac} is low (10^{-9} $(\Omega\ \text{cm})^{-1}$) at $T <$ 150 K. At $T \sim$ 150 K, σ_{loc} along these axes rises abruptly and exist up to room temperature without a noticeable change. This means that the itinerant electrons which appear at $T >$ 150 K because σ_{loc} along the b axis vanish are localized anew and enhance σ_{loc} along the a and c axes. As temperature further grows, the frequency dispersion of σ_{loc} along the a and c axes begins to decrease due to the leakage growth. P^{rem} along the a and c axes is screened by leakage rather sharply when the leakage and local conductivities become comparable. Thus, σ_{loc} and leakage anisotropy we observed is consistent with the T_{scr} magnitudes for P^{rem} along different axes.

A specific situation arises along the b axis. Near 30 K, the maximum in P^{rem} corresponding to the low-temperature ferroelectric transition caused by exchange striction is observed against the background of the $P_b^{rem}(T)$ dependence (see the right panel in Fig. 2b). Note that P_b^{rem} is much lower than $P_b =$ 0.26 μC/cm^2 at $T <$ 30 K which was measured by the pyrocurrent method in the same sample at $E = 0$ [16]. The application of the uniform polarizing field $E =$ ±2.7 kV/cm reduced insignificantly P_b and did not lead to its reversal when the sign of E was changed (see Fig. 1 in [16]). We attributed this to the fact that P_b arose in the internal non-uniform electric field caused by the ferromagnetic and antiferromagnetic $Mn^{3+}-Mn^{4+}$ ion pairs alternating along the b axis (the exchange striction mechanism [7]). This suggests that the low temperature polarization response to a weak field E (compared with the internal field) should be low. Near T_C, when the internal field begins to decrease and disappears and the P_b fluctuations increase, the response to the field E is observed as a maximum against the background of $P_b^{rem}(T)$. Near $T_C \approx$ 30 K the dispersion-free anomalies typical of the ferroelectric phase transition manifest themselves against the background of σ_{loc} and σ_{ac} along the b axis (see Fig. 3) because a maximum in ε" should be observed near T_C. As a result, two different polarizations coexist along the b axis: the low-temperature polarization (up to 30 K) caused by exchange striction and the polarization caused by the RPD (up to 100 K).

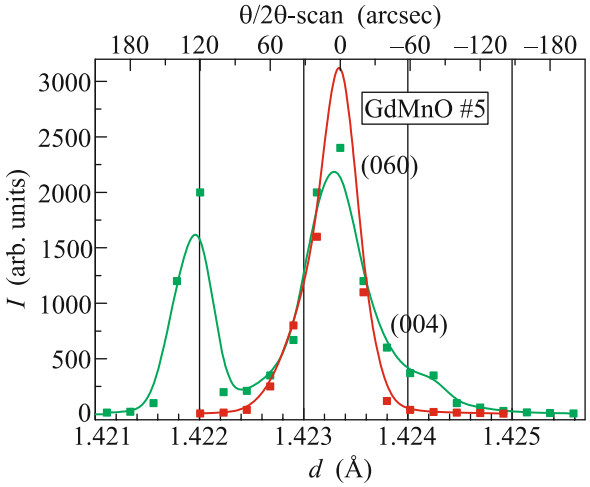

Fig. 4. (Color online) Angular intensity distributions of (004) and $(060)_{CuK\alpha 1}$ Bragg reflections as functions of interplanar distances d. The lattice parameters are $a =$ (7.3568 ± 2) Å; $b =$ (8.5398 ± 2) Å; $c =$ (5.6920 ± 2) Å.

The effect of the longitudinal magnetic field H on the hysteresis loops was also studied. As one can see from the right panels in Fig. 2, the field H increases both P^{rem} and T_{scr} along the b axis and only T_{scr} along the a and c axes.

The X-ray high-sensitivity diffraction study was carried out at room temperature (see Fig. 4). The angular intensity distributions of (004) and $(060)_{CuK\alpha 1}$ Bragg reflections were detected in the three-crystal regime with the θ/2θ scan. As a monochromator and an analyzer, germanium crystals in the (004) reflection were used, which allowed conditions of nearly dispersion-free high-resolution (~2″) survey geometry to be realized. Figure 4 shows a single diffraction maximum of (060) and two diffraction maxima of the (004) Bragg reflections recorded from different single crystal planes perpendicular to the b and c axes, respectively. The (004) Bragg reflection positions are characterized by slightly different interplanar spacings d ($\Delta d \approx$ 0.0015 Å). These (004) reflections, which have comparable intensities and half-width (~20″) clearly point to a coexistence of two phases with slightly different c lattice parameters, which differ only in the third decimal place. The Bragg peak along the b axis with a similar half-width is not split, i.e., it is identical

to these two phases. The positions of all Bragg peaks nearly coincide with the positions for the GMO with the generally accepted *Pbam* symmetry. This means that two phases we detected are high-quality GMO single crystal phases with similar large correlation lengths R_c. The phase with a higher intensity of the (004) Bragg peak can be attributed to the original matrix. The phase with a lower intensity of such peak can be attributed to the RPD.

The GMO state related to the RPD in the original matrix is an analog of the superparaelectric state formed by an ensemble of spherical ferroelectric nanoparticles (in our case RPD) in a dielectric matrix. It was theoretically studied in [25] where it was shown that at low temperatures a homogeneous polarization could exist in RPD if their sizes R were less than the correlation radius R_c but larger than the critical radius R_{cr} of the size-driven ferroelectric-paraelectric phase transition. Under these conditions, all dipole moments inside RPD are aligned due to correlation effects. Surface screening of depolarization fields makes the RPD single-domain states energetically favorable. If $R < R_{cr}$, separate paraelectric dipoles are uncorrelated and represent local polar defects which can only increase the width of the original matrix Bragg peak. The fact that the well-defined Bragg reflection related to the RPD observed in our study together with the similar Bragg peak of the original matrix indicates that the conditions for the ferroelectric RPD emergence given in [25] are fulfilled. At room temperature, the volumes of these phases are similar. The coexistence of the two phases was observed in our X-ray diffraction studies of several GMO single crystals, as well as another RMn_2O_5 crystal ($EuMn_2O_5$) [12, 13]. Thus, we can conclude that the coexistence of these phases is an intrinsic property of the crystals studied attributable to phase separation.

Let us consider in more detail what RPD are. There is a probability that e_g electrons of some Mn^{3+} ions tunnel to Mn^{4+} ions in the original GMO matrix. These valence electrons and recharged Mn^{3+}-Mn^{4+} ion pairs are accumulated in the RPD inside the original matrix due to the fact that phase separation is energetically favorable [9, 10]. Since Mn^{3+} ions appear in the Mn^{4+} ion positions (i.e., in the octahedral oxygen surrounding), they become Jahn–Teller ions and give rise to local deformations of these octahedra. In turn, Mn^{4+} ions appear in the Mn^{3+} ion positions (in noncentrosymmetric pentagonal pyramids) and local distortions arise near these ions as well. As a result, structural distortions caused by both these factors occur inside RPD. We believe that RPD are noncentrosymmetric and their sizes are consistent with the conditions for the emergence of ferroelectric single-domain states given above. The self-consistency between the RPD and the initial matrix leads to the noncentrosymmetricity of the entire crystal.

Since P–E hysteresis loops are measured under the field E applied along different axes, electric polarizations are induced along these axes, making it impossible to select the crystal symmetry from those proposed in [8]. Indeed, the application of field E in a certain direction initiates a drift of valence e_g electrons localized inside RPD. These electrons recharge Mn^{3+} and Mn^{4+} ions in RPD. As a result, the spatial distribution of the Mn^{3+} and Mn^{4+} ions and structural distortions inside RPD are bound to change, giving rise to the polarization along the E direction. Thus, the actual symmetry of GMO at room temperature can be established only in polarization measurements in $E = 0$.

Phase separation and charge carrier self-organization give rise to a dynamic equilibrium of the RPD states with a balance between attraction (double exchange, Jahn–Teller effect) and Coulomb repulsion of charge carriers [9, 10, 12]. The formation of the RPD due to a balance between strong interactions leads to specific features in GMO properties. First, the polar RPD are bound to emerge up to high temperatures, thus giving rise to high-temperature polarization. Second, the changes in RPD under varying E rapidly restore to the dynamic equilibrium states after E is switched off. These features were observed in our experiments.

The application of magnetic field H increases the barriers at the RPD boundaries due to the double exchange growth, thus increasing the T_{scr} temperatures (see the right panels in Fig. 2). The field H oriented along the b axis also enhances the polarization induced by the RPD due to increasing of the probability of charge transfer between Mn^{3+}–Mn^{4+} ion pairs with the greatest distance between them (see the capture in Fig. 4).

As found in [25], a frozen superparaelectric phase can emerge for an ensemble of spherical ferroelectric nanoparticles in a dielectric matrix. In this phase, P^{rem} and the hysteresis loop arise at the temperatures lower than the freezing temperature T_f. The temperature T_f was defined from the condition that the potential barriers of nanoparticle polarization reorientation become equal to the thermal activation energy $\sim k_B T$. At $T > T_f$, the conventional superparaelectric state occurs. It was also accepted in [25] that the temperature of thermal destruction of intrinsic nanoparticle ferroelectricity is $T_{cr} \gg T_f$. As a result, the temperature behavior of the GMO polarization is also analogous to that of the frozen superparaelectric state discussed in [25]. The temperature T_{scr} considered above can be regarded as T_f. Indeed, σ_{loc} must exceed leakage at $T < T_{scr}$, while the thermally activated leakage must dominate at $T > T_{scr}$.

Thus, the remanent polarizations and hysteresis loops, originating from the frozen superparaelectric state of similar ferroelectric RPD, which are arranged inside the initial matrix of GMO, are revealed in the

paramagnetic phase. The polarization along the *c* axis is detected up to room temperature. The RPD emerge due to phase separation and charge carrier self-organization. The polarization observed can be attributed to the magnetically induced polarization since the magnetic double exchange is the key interaction giving rise to the RPD formation. The effect of magnetic field on the polarization demonstrates that the magnetoelectric coupling exists in the paramagnetic phase.

This work was supported by the Government of Russian Federation (project no. 0.14.B25.31.0025) and partly by the Presidium of the Russian Academy of Sciences (program P2).

REFERENCES

1. T. Kimura, T. Goto, H. Shintani, K. Ishizaka, and Y. Tokura, Nature (London) **426**, 55 (2003).
2. N. Hur, S. Park, P. A. Sharma, J. S. Ahn, S. Guba, and S.-W. Cheong, Nature (London) **429**, 392 (2004).
3. H. Katsura, N. Nagaosa, and A. V. Balatsky, Phys. Rev. Lett. **95**, 057205 (2005).
4. M. Mostovoy, Phys. Rev. Lett. **96**, 067601 (2006).
5. Y. Noda, H. Kimura, M. Fukunaga, S. Kobayashi, I. Kagomiya, and K. Kohn, J. Phys.: Condens. Matter **20**, 434206 (2008).
6. P. G. Radaelli and L. C. Chapon, J. Phys.: Condens. Matter **20**, 434213 (2008).
7. J. Van den Brink and D. J. Khomskii, J. Phys.: Condens. Matter **20**, 434217 (2008).
8. V. Baledent, S. Chattopadhyay, P. Fertey, M. B. Lepetit, M. Greenblatt, B. Wanklyn, F. O. Saouma, J. I. Jang, and P. Foury-Leylekian, Phys. Rev. Lett. **114**, 117601 (2015).
9. L. P. Gor'kov, Phys. Usp. **41**, 589 (1998).
10. M. Yu. Kagan and K. I. Kugel, Phys. Usp. **44**, 553 (2001).
11. P. G. de Gannes, Phys. Rev. **118**, 141 (1960).
12. V. A. Sanina, E. I. Golovenchits, V. G. Zalesskii, S. G. Lushnikov, M. P. Scheglov, S. N. Gvasaliya, A. Savvinov, R. S. Katiyar, H. Kawaji, and T. Atake, Phys. Rev. B **80**, 224401 (2009).
13. V. A. Sanina, E. I. Golovenchits, V. G. Zalesskii, and M. P. Scheglov, J. Phys.: Condens. Matter **23**, 456003 (2011).
14. E. I. Golovenchits, V. A. Sanina, and V. G. Zalesskii, JETP Lett. **95**, 386 (2012).
15. V. A. Sanina, E. I. Golovenchits, and V. G. Zalesskii, J. Phys.: Condens. Matter **24**, 346002 (2012).
16. V. A. Sanina, E. I. Golovenchits, B. Kh. Khannanov, M. P. Scheglov, and V. G. Zalesskii, JETP Lett. **100**, 407 (2014).
17. B. Kh. Khannanov, V. A. Sanina, and E. I. Golovenchits, J. Phys.: Conf. Ser. **572**, 012046 (2014).
18. N. Lee, C. Vecchini, Y. J. Choi, L. C. Chapon, A. Bombardi, P. G. Radaelli, and S. W. Cheong, Phys. Rev. Lett. **110**, 137203 (2013).
19. V. A. Sanina, L. M. Sapozhnikova, E. I. Golovenchits, and N. V. Morozov, Sov. Phys. Solid State **30**, 1736 (1988).
20. E. I. Golovenchits, N. V. Morozov, V. A. Sanina, and L. M. Sapozhnikova, Sov. Phys. Solid State **34**, 56 (1992).
21. J. F. Scott, L. Kammerdiner, L. M. Parris, S. Traynor, V. Ottenbacher, A. Shawabkeh, and W. F. Oliver, J. Appl. Phys. **64**, 787 (1988).
22. M. Fukunaga and Y. Noda, J. Phys. Soc. J. **77**, 064706 (2008).
23. S. M. Feng, Y. S. Chai, J. L. Zhu, N. Manivannan, Y. S. Oh, L. J. Wang, Y. S. Yang, C. Q. Jin, and K. H. Kim, New J. Phys. **12**, 073006 (2010).
24. A. R. Long, Adv. Phys. **31**, 587 (1982).
25. M. D. Glinchuk, E. A. Eliseev, and A. N. Morozovska, Phys. Rev. B **78**, 134107 (2008).